

Nuclear quantum effects on the hydrogen bond donor–acceptor exchange in water–water and water–methanol dimers

Cite as: J. Chem. Phys. **153**, 054302 (2020); <https://doi.org/10.1063/5.0016122>

Submitted: 02 June 2020 . Accepted: 13 July 2020 . Published Online: 03 August 2020

Emilio Méndez , and Daniel Laria 



View Online



Export Citation



CrossMark

Lock-in Amplifiers
up to 600 MHz



Watch



Nuclear quantum effects on the hydrogen bond donor-acceptor exchange in water-water and water-methanol dimers

Cite as: J. Chem. Phys. 153, 054302 (2020); doi: 10.1063/5.0016122

Submitted: 2 June 2020 • Accepted: 13 July 2020 •

Published Online: 3 August 2020



View Online



Export Citation



CrossMark

Emilio Méndez¹  and Daniel Laria^{1,2,a)} 

AFFILIATIONS

¹Departamento de Química Inorgánica Analítica y Química-Física e INQUIMAE, Facultad de Ciencias Exactas y Naturales, Universidad de Buenos Aires, Ciudad Universitaria, Pabellón II, 1428 Buenos Aires, Argentina

²Departamento de Física de la Materia Condensada, Comisión Nacional de Energía Atómica, Avenida Libertador 8250, 1429 Buenos Aires, Argentina

^{a)}Author to whom correspondence should be addressed: dhlaria@cnea.gov.ar

ABSTRACT

We present results from path integral molecular dynamics simulations that describe effects from the explicit incorporation of nuclear quantum fluctuations on the topology of the free energy associated with the geared exchange of hydrogen bonds in the water-water dimer. Compared to the classical treatment, our results reveal important reductions in the free energy barriers and changes at a qualitative level in the overall profile. Most notable are those manifested by a plateau behavior, ascribed to nuclear tunneling, which bridges reactant and product states, contrasting with the usual symmetric double-well profile. The characteristics of the proton localizations along the pathway are examined. An imaginary time analysis of the rotational degrees of freedom of the partners in the dimer at the vicinities of transition states shows a clear “anticorrelation” between intermolecular interactions coupling beads localized in connective and dangling basins of attractions. As such, the transfer is operated by gradual concerted inter-basin migrations in opposite directions, at practically no energy costs. Modifications operated by partial deuteration and by the asymmetries in the hydrogen bonding characteristics prevailing in water-methanol heterodimers are also examined.

Published under license by AIP Publishing. <https://doi.org/10.1063/5.0016122>

I. INTRODUCTION

The water dimer represents the simplest aqueous moiety exhibiting hydrogen bonded (HB) intramolecular connectivity. The direct inspection of the nuclear arrangement corresponding to the global minimum of its potential energy surface, characterized by a practically linear O–H···O arrangement, clearly reveals one key characteristic of the intermolecular connectivity of water, i.e., the high degree of orientational correlation that prevails between donor and acceptor partners. This correlation, observed in the gas phase, persists to a non-negligible extent in liquid environments at temperatures well beyond ambient conditions, representing the cornerstone of the distinctive tetrahedral coordination of the individual molecules with their nearest neighbors.

Despite the apparent simplicity of the latter description, the landscape of the underlying potential energy surface controlling

nuclear configurations in the dimer presents a series of interesting features. Most notable is the collection of eight isoenergetic local minima, each one describing non-superimposable configurations obtained by site-permutations of the H-nuclei, without breaking intramolecular bonds.^{1,2} Transitions between these local minima involve large amplitude tunneling motions, which are clearly manifested in the rich variety of signals that appear in the far-infrared branch of the cluster spectra. Adequate interpretations of these rovibrational signals were made possible by the advent of a series of sophisticated spectroscopic techniques such as ringdown laser absorption spectroscopy^{3,4} and terahertz vibration-rotation tunneling spectroscopy,⁵ to cite two relevant examples.

From a theoretical perspective, several formalisms have also been successfully devised to provide adequate rationalizations of the experimental tunneling signals.⁶ Without being exhaustive, the list includes diagonalization techniques,⁷ diffusion Monte Carlo,⁸

time evolution methods,⁹ path-integral techniques,¹⁰ flip analysis,¹¹ quantum calculations,¹² and, more recently, instanton based methodologies.^{13–19} Moreover, experimental spectra also served as appropriate test benchmarks to validate predictions from highly accurate force fields.^{20,21}

Coming back to the consideration of the characteristics of the dimer potential energy surface, the gross features describing the reactive pathways connecting the different local minima are normally cast in terms of three different collective modes: (i) the first one corresponds to the positional exchange of the two protons in the acceptor molecule; (ii) bifurcation events represent a second kind of pathway along which the H-exchange takes place in the donor partner; and (iii) the third category corresponds to isomerization processes where the two partners of the pair interchange their original HB donor and acceptor roles. These transitions can evolve via geared and anti-geared coordinated rotations. In the three cases, trajectories joining reactant and product configurations include passages over relatively low energy tunneling barriers; quantum calculations show that barrier heights for the last pathways are intermediate between the corresponding values of the other two channels.⁶

In what follows, we will concentrate on the examination of the latter mode from a complementary perspective. More specifically, our interest here will be centered in the analysis of the combined effects of quantum and thermal fluctuations that modulate the characteristics of the free energy profile projected along a collective coordinate describing the HB exchanges in the water–water (W–W) dimer. In addition, we also explore asymmetries in the free energy profiles introduced by partial deuteration and by analyzing heterodimers combining partners with different HB acceptor and donor characteristics, such as the water–methanol (W–MeOH) case. In a more general context, the analysis of these free energy profiles provides important information with direct implications in both equilibria and dynamical characteristics of nanoclusters. On the one hand, the imbalances between the corresponding free energy values assigned to reactants and products determine chemical equilibria between different conformers, which can be clearly detected in the corresponding intensities of spectroscopic signals.^{22–24} On the other hand, the magnitudes of free energy barriers determine reaction rates for interconversions and provide elements to determine relative prevalences of classical, i.e., over-the-barrier, vs tunneling-controlled mechanisms of the reactive paths. Our description will rely on results from Path-Integral Molecular Dynamics (PIMD) simulations.

The organization of the presentation is as follows: in Sec. II, we briefly overview details of the model and the simulation procedure. The main results of our simulations are presented in Sec. III. Finally, the main conclusions of this article are recapitulated in Sec. IV.

II. MODEL AND SIMULATION PROCEDURES

The systems under investigation consisted of W–W and W–MeOH dimers at cryogenic conditions, spanning the 20 K–50 K temperature interval. Nuclear quantum fluctuation effects were analyzed by running standard PIMD simulation runs.^{25,26} The latter scheme exploits the well known isomorphism²⁷ that can be established between quantum statistical mechanics and the classical treatment of harmonic cyclic-polymers, via an appropriate

P -discretization of the canonical partition function. As such, for an N particle system with coordinates $\{\mathbf{r}_N\}$, at a temperature T , and with potential energy $V(\{\mathbf{r}_N\})$, expectation values of position dependent observables $\mathcal{O}(\{\mathbf{r}_N\})$ can be computed as

$$\langle \mathcal{O} \rangle = \lim_{P \rightarrow \infty} \left\langle \frac{1}{P} \sum_{k=1}^P \mathcal{O}(\{\mathbf{r}_N^{(k)}\}) \right\rangle_{H_P}, \quad (1)$$

where $\langle \dots \rangle_{H_P}$ denotes a statistical average collected along molecular dynamics trajectories generated by the following Hamiltonian:

$$H_P(\{\mathbf{p}_i^{(k)}\}, \{\mathbf{r}_i^{(k)}\}) = \sum_{i=1}^N \sum_{k=1}^P \left[\frac{(\mathbf{p}_i^{(k)})^2}{2M_i} + \frac{M_i P}{2(\beta\hbar)^2} (\mathbf{r}_i^{(k)} - \mathbf{r}_i^{(k+1)})^2 \right] + \frac{1}{P} \sum_{k=1}^P V(\mathbf{r}_1^{(k)}, \mathbf{r}_2^{(k)}, \dots, \mathbf{r}_N^{(k)}). \quad (2)$$

In the previous equation, $\beta^{-1} = k_B T$, and $\mathbf{r}_i^{(k)}$ and $\mathbf{p}_i^{(k)}$ denote the position and momentum of the i th particle of mass M_i evaluated at the k th imaginary time slice, respectively.

The potential energy describing W–W interactions were modeled with the non-harmonic, q-TIP4P/F flexible model developed by Habershon *et al.*²⁸ This force field was originally designed to provide adequate descriptions of nuclear quantum effects on several static and dynamical properties of bulk water. Its direct implementation to model cluster environments is also known to provide reasonable descriptions,^{29,30} although it overestimates binding energies when compared to much more sophisticated models.^{10,31} In order to provide a unified level of description of all interactions, for MeOH, we implemented a modified version of a similar, non-harmonic potential, developed by Homna *et al.*³² The modifications operated in the original parameterization included the incorporation of a full atom description of the methyl group and minor changes of some parameters so as to reproduce characteristics of the gas phase infrared spectrum of the MeOH monomer. Full details of the model and the spectrum calculations can be found in the [supplementary material](#). On the other hand, W–MeOH cross interactions were modeled by implementing the usual arithmetic and geometric means for the length and energy Lennard-Jones parameters, respectively.

The thermodynamic information that will be presented in what follows was collected along simulation runs that included a transformation from Cartesian to normal mode coordinates,^{33,34} coupled to a multiple time step algorithm³⁵ that differentiated fast intramolecular and intrapolymer interactions from the rest of the slowly variant, Lennard-Jones and Coulomb contributions. The long time step was set to $\Delta t = 0.1$ fs, while the short one was $\delta t = \Delta t/3$. The number of beads was set to $P = 256$. A few test runs performed with a number of beads twice as large showed differences in the computed averages that never exceeded $\sim 2\%$. Appropriate thermal control along the runs was obtained by coupling each component of each tagged n th polymer-normal mode with frequency ω_n to a chain of three Nosé–Hoover thermostats with masses set at $Q_n = (\beta\omega_n^2)^{-1}$.³⁶

III. RESULTS

A. Water dimers

We will start our analysis by examining the characteristics of a collective mode that describes isomerization paths along which two

molecules comprising a W–W dimer interchange their hydrogen-bond donor/acceptor roles, namely,



In the previous equation, the subscripts identify atoms in a tagged member of the dimer, whereas the superscripts *con* and *dng* denote hydrogen atoms at connecting and dangling positions, respectively [see the sequence (a) through (c) on the left-hand side of Fig. 1].

Following a previous analysis,³⁷ we found it useful to consider a simple order parameter, $\xi_{fp}(\{\mathbf{r}_N\})$, that clearly allowed us to discriminate reactant from product states in the previous expression. Based on simple geometrical considerations, the latter magnitude was defined in terms of the subtraction of two angular variables describing individual flippings [see Fig. 1(b)] as follows:

$$\xi_{fp}(\{\mathbf{r}_N\}) = \cos \theta_2(\{\mathbf{r}_N\}) - \cos \theta_1(\{\mathbf{r}_N\}), \quad (4)$$

where

$$\cos \theta_1 = \frac{\mathbf{r}_{\text{H}_1\text{O}_1} \cdot \mathbf{r}_{\text{O}_2\text{O}_1}}{|\mathbf{r}_{\text{H}_1\text{O}_1}| |\mathbf{r}_{\text{O}_2\text{O}_1}|} \quad (5)$$

and

$$\cos \theta_2 = \frac{\mathbf{r}_{\text{H}_2\text{O}_2} \cdot \mathbf{r}_{\text{O}_1\text{O}_2}}{|\mathbf{r}_{\text{H}_2\text{O}_2}| |\mathbf{r}_{\text{O}_1\text{O}_2}|}. \quad (6)$$

In the previous expressions, $\mathbf{r}_{\alpha\gamma} = \mathbf{r}_\alpha - \mathbf{r}_\gamma$ and \mathbf{r}_α denotes the coordinate of a tagged atom α . From these definitions, reactant states in Eq. (3) are characterized by values of ξ close to or below -1 , whereas product states are characterized by values of ξ close to or beyond 1 .

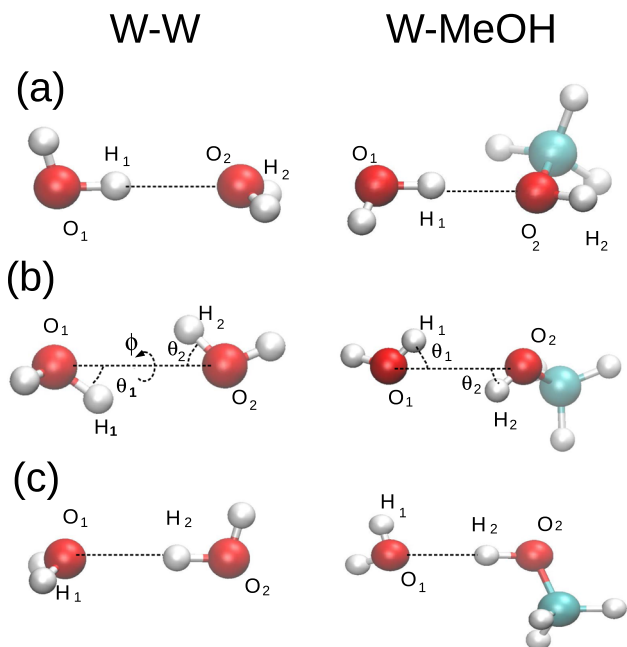


FIG. 1. Snapshots of representative configurations of W–W (left-hand side) and W–MeOH (right-hand side) dimers at different stages of the geared HB exchange isomerization: (a) reactant state, (b) transition state, and (c) product state.

The construction of the free energy profile $A(\xi)$ along the reactive path dictated by ξ represented the next step of our analysis,

$$-\beta A(\xi^\dagger) \propto \ln \langle \delta(\xi(\{\mathbf{r}_N\}) - \xi^\dagger) \rangle, \quad (7)$$

where $\langle \dots \rangle$ denotes a statistical average. In consonance with Eq. (1), the implementation of the latter expression within the path-integral formalism is straightforward and the resulting expression is the following “bead average”:

$$-\beta A(\xi') \propto \ln \left[\frac{1}{P} \sum_{k=1}^P \langle \delta(\xi(\{\mathbf{r}_N^{(k)}\}) - \xi') \rangle \right]. \quad (8)$$

Unfortunately, the implementation of the latter expression presented important statistical noise when the sampling required the use of non-Boltzmann biasing tools, as we will describe shortly. As a reasonable alternative, considering the natural correspondence between nuclear positions and centroid coordinates, we adopted a classical-like expression expressed in terms of nuclear centroids,

$$-\beta A(\xi') \propto \ln \langle \delta(\xi(\{\mathbf{r}_N^{\text{cnt}}\}) - \xi') \rangle, \quad (9)$$

where

$$\mathbf{r}_\alpha^{\text{cnt}} = \frac{1}{P} \sum_{k=1}^P \mathbf{r}_\alpha^{(k)}. \quad (10)$$

The expression in Eq. (9), albeit an approximate one, does not present convergence problems, and it is known to yield reasonable estimates.

Flipping episodes involve partial ruptures and reconstructions of hydrogen bonds that, in the gas phase, require energy costs of the order of 3 kcal mol^{-1} – 4 kcal mol^{-1} . Consequently, at cryogenic temperatures below, say, 100 K , such interconversions represent rare events. As such, proper sampling along the relevant phase space normally requires the implementation of some kind of biased sampling scheme. For this case, we found that the incorporation of additional harmonic umbrella sampling potentials of the type³⁸

$$V_i^{\text{bias}}(\{\mathbf{r}_N^{\text{cnt}}\}) = k_{\text{bias}} [\xi(\{\mathbf{r}_N^{\text{cnt}}\}) - \xi_i]^2 \quad (11)$$

was sufficient to provide adequate sampling along the complete ξ interval of interest described by the exchange path. In the present case, we used 10 overlapping windows centered at equidistant ξ_i values and harmonic constants k_{bias} set at typical values of the order of $\sim 3 \text{ kcal mol}^{-1}$ – 4 kcal mol^{-1} . In passing, we note that a rigorous treatment of umbrella potentials within path-integral schemes requires the implementation of either P -different biasing potentials or, alternatively, a single one applied on a tagged bead.³⁹ Although the latter procedure has been successfully implemented to treat free energy profiles characterized by a single minimum, all our attempts to reconstruct free energy profiles with double-well characteristics showed important convergence problems.

Plots for $A(\xi)$ corresponding to PIMD simulations performed at $T = 50 \text{ K}$ and at $T = 20 \text{ K}$ are displayed in Fig. 2. As a reference, we have also included results from classical simulations with solid symbols. In all cases, the curves are symmetric, with reactant and product states characterized by values of $\xi \sim \pm 1.4$ and separated

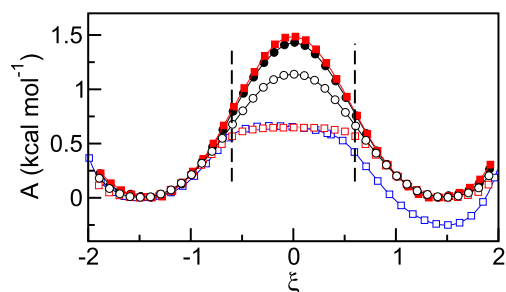


FIG. 2. Free energy profiles associated with the hydrogen bond donor/acceptor interchange for the water dimer. Red curves: $T = 50$ K; black curves: $T = 50$ K; blue curve: results for a partially deuterated dimer at $T = 20$ K. Solid symbols correspond to classical results, whereas open symbols correspond to path-integral results. The vertical lines indicate boundaries between quadratic and tunneling regimes.

by barriers centered at the $\xi = 0 = \xi^\ddagger$ transition state. Typical configurations for the reactant/product states exhibit roughly collinear alignments of the $\text{O}_i\text{H}_i^{\text{con}}\dots\text{O}_j$ centroids and values of θ_j close to 115° . On the other hand, configurations corresponding to transition states are characterized by practically coplanar arrangements of the centroids of the four atoms involved in the definition of the order parameter. For example, at $T = 20$ K, we registered $\langle \cos \phi \rangle = -0.9 \pm 0.1$, where ϕ corresponds to the $\text{H}_1\text{-O}_1\text{-O}_2\text{-H}_2$ dihedral angle [see left panel (b) of Fig. 1], and $\langle \cos \theta_i \rangle = 0.67 \pm 0.07$ for $i = 1, 2$. As such, the biased potential scheme naturally drove the sampling along the geared exchange collective mode pathway.

At both temperatures, the incorporation of nuclear quantum fluctuations promotes sensible reductions in the magnitudes of the free energy barriers separating reactant from product states. Contrasting with the virtually constant $\Delta A^\ddagger \sim 1.45$ kcal mol $^{-1}$ values of the classical barrier energies, the quantum estimate at $T = 50$ K is reduced by a factor of 0.8 and by a factor of approximately one half at $T = 20$ K. We also remark that, although at the first glance, all plots could be described in terms of standard double-well profiles, the curve for $T = 20$ K flattens considerably at the vicinities of the transition state, exhibiting sharp transitions at $\xi \sim \pm 0.5$ between quadratic-like and practically plateau-like behaviors.

Looking for key elements that would allow a physical interpretation of the latter characteristics, we analyzed the behaviors of a series of observables along the interconversion process. More specifically, we are referring to conditional averages of the type

$$\langle \text{O} \rangle_{\xi=\xi'} = \frac{\langle \text{O}(\{\mathbf{r}_N\}) \delta(\xi - \xi') \rangle}{\langle \delta(\xi - \xi') \rangle} \quad (12)$$

for different values of ξ' along the reaction path. The first magnitude that we considered was the difference between classical and quantum estimates for the free energies associated with transition and reactant/product states. We are referring to the following magnitude:

$$\Delta A_{\xi'}^{\text{cl} \rightarrow \text{qn}} = \int_0^1 d\lambda A_{\xi'}^{\text{SC}}(\lambda), \quad (13)$$

where the integrand in the previous expression is given by⁴⁰

$$A_{\xi'}^{\text{SC}}(\lambda) = \frac{1}{P} \sum_{i=1}^N \sum_{k=1}^P \left\langle \left(\mathbf{r}_i^{(k)} - \mathbf{r}_i^c \right) \frac{\partial V(\{\tilde{\mathbf{r}}_i^{(k)}\})}{\partial \tilde{\mathbf{r}}_i^{(k)}} \right\rangle_{\xi=\xi', \lambda} \quad (14)$$

The second subindex λ in Eq. (14) denotes an average collected along trajectories controlled by the following scaled Hamiltonian:

$$H_P^{\text{SC}}(\lambda) = \sum_{i=1}^N \sum_{k=1}^P \left[\frac{(\mathbf{p}_i^{(k)})^2}{2M_i} + \frac{M_i P}{2(\beta\hbar)^2} (\mathbf{r}_i^{(k)} - \mathbf{r}_i^{(k+1)})^2 \right] + \frac{1}{P} V(\{\tilde{\mathbf{r}}_i^{(k)}\}), \quad (15)$$

with

$$\tilde{\mathbf{r}}_i^{(k)} = \lambda \mathbf{r}_i^{(k)} + (1 - \lambda) \mathbf{r}_i^{\text{cnt}}. \quad (16)$$

For the stable reactant/product states, at $T = 20$ K, we registered a $\Delta A_{\xi'=\pm 1.5}^{\text{cl} \rightarrow \text{qn}} = 21.4 \pm 0.4$ kcal mol $^{-1}$ free energy difference, whereas, at the transition state, the change in free energy was found to be $\Delta A_{\xi'=0}^{\text{cl} \rightarrow \text{qn}} = 20.7 \pm 0.6$ kcal mol $^{-1}$. The difference between these two results leads to a net change in ΔA^\ddagger between the classical and quantum estimates of $[\Delta A^\ddagger]^{\text{cl} \rightarrow \text{qn}} = \Delta A_{\xi'=0}^{\text{cl} \rightarrow \text{qn}} - \Delta A_{\xi'=\pm 1.5}^{\text{cl} \rightarrow \text{qn}} = -0.7$ kcal mol $^{-1}$, a value that agrees reasonably well with the -0.75 kcal mol $^{-1}$ difference obtained by implementing the biased sampling scheme.

The results for the evolution of the individual rotations of the $\text{O}_i\text{-H}_i$ bonds are presented in the bottom panel of Fig. 3 with red curves. Note that along the $\xi \lesssim -0.7$ stage, the angular displacements of the H_i -centroids evolve at different paces: the net change for the dangling H_2 atom along this stage is $\Delta \cos \theta_2 \sim 0.7$, whereas

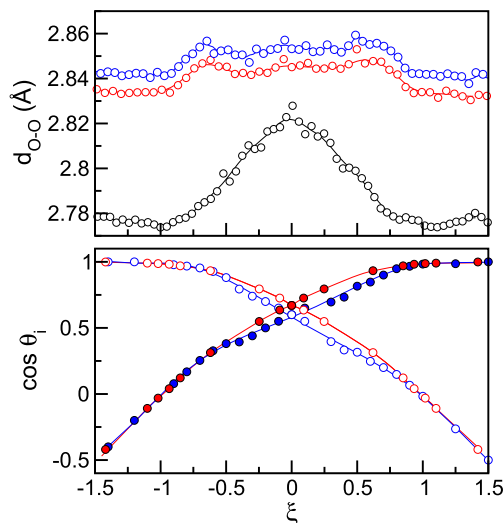


FIG. 3. Evolution of different geometrical parameters along the HB donor/acceptor exchange path. Bottom panel: individual rotations in W-W (red curves) and W-MeOH (blue curves) dimers. Open symbols: $\cos \theta_1$ and solid symbols: $\cos \theta_2$. Top panel: $\text{O}_1\text{-O}_2$ distance evolutions in W-W dimers. Red circles: bead-to-bead distance; blue circles: centroid-to-centroid distance; and black circles: classical results.

for the connecting H_1 atom, that value is only $\Delta \cos \theta_1 \sim -0.1$, preannouncing the tighter confining characteristics prevailing at connecting positions that will be described later. Yet, the two sweep rates become much more comparable as $\cos \theta_2$ attains ~ 0.25 ($\theta_2 \sim 75^\circ$), remaining so as the interconversion evolves toward the transition state.

The changes operated in the O_1 – O_2 distance along the reactive path are presented in the top panel of Fig. 3. In all cases, the modifications do not exceed a few hundredths of Angstroms. Along the $\xi < 0$ interval, the classic treatment yields a curve exhibiting a steady ~ 0.05 Å increment that roughly reproduces the characteristics of the corresponding free energy. On the other hand, the quantum counterparts show even milder modifications, suggesting the weak nature of the coupling between the collective rotations and the tagged O – O intermolecular stretching mode. Yet, note that the plateau-like behavior observed in the quantum free energy can also be detected here along the $|\xi| \lesssim 0.7$ interval. The comparison between mean values corresponding to centroid-to-centroid and bead-to-bead O_1 – O_2 distances reveals small shifts toward smaller values in the latter values.

Bead statistics provide additional insights that complete our description. The plots on the left panel of Fig. 4 correspond to the results for the imaginary time mean square displacements for the tagged H_i -atoms,

$$\mathcal{R}_i^2(k; \xi) = \frac{1}{P} \sum_{j=1}^P \left| \mathbf{r}_{H_i}^{(j+k)} - \mathbf{r}_{H_i}^{(j)} \right|_\xi^2. \quad (17)$$

The characteristics of the plots at the reactant state contrast sharply with the one observed at the transition state. In particular,

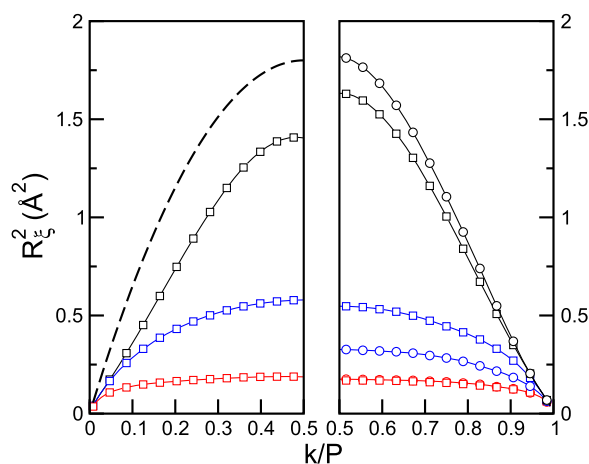


FIG. 4. Imaginary time mean square displacement for different hydrogen atoms in W–W (left panel) and W–MeOH (right panel) dimers at $T = 20$ K. Black symbols correspond to sampling at the vicinity of the transition states. Blue and red symbols correspond to atoms at dangling and connective positions at stable states, respectively. Squares correspond to H_1 atoms, and circles correspond to H_2 atoms [see Eqs. (1) and (22)]. In the right panel, red symbols are indistinguishable in the scale of the figure. The dashed line corresponds to results for thermalized, non-interacting protons. For clarity purposes, in both panels, only half of the imaginary time intervals are displayed.

note the disparity in the corresponding correlation lengths computed from the values of $\mathcal{R}_i(k = P/2; \xi)$, which provide rough estimates for the overall quantum dispersions of the protons along the reactive path. Combined effects from the particular local characteristics of the intramolecular and intermolecular Coulomb-coupling provoke stronger localizations of protons located at connecting positions (blue squares) compared to those registered at dangling positions (red squares). The near constancy of the plot for the connective protons along the whole imaginary time interval reveals a clear signal of ground state dominance⁴¹ and indicates that the overall shape of the isomeric polymers can be portrayed in terms of a closely packed moiety of ~ 0.3 Å diameter. As we mentioned, dangling protons look somewhat more delocalized, and their corresponding spatial descriptions include a larger variety of characteristic length scales spanning up to ~ 0.7 Å. Much more dramatic modifications of the proton-polymer shape are operated at the vicinity of the transition state, where the correlation length becomes comparable to the value for the thermalized, free (i.e., non-interacting) proton,⁴¹ indicated by the dashed line in Fig. 4: $\mathcal{R}_i(k = P/2; \xi = 0) = 0.9 \times \mathcal{R}_{free} = 1.2$ Å.

A more vivid characterization of the latter proton delocalization can be obtained from spatial bead densities. Exploiting the already mentioned, quasi-perfect coplanar arrangement of the centroids at the transition state, we found it illustrative to compute the following two-dimensional distribution:

$$\rho_{2D}(x, y) = \frac{1}{P} \sum_{i=1}^2 \sum_{k=1}^P \langle \delta(x_{H_i}^{(k)} - x) \delta(y_{H_i}^{(k)} - y) \rangle_{\xi=0}, \quad (18)$$

where $x_{H_i}^{(k)}$ and $y_{H_i}^{(k)}$ denote the coordinates of the k th bead of proton H_i measured with respect to a local coordinate system centered at the midpoint between the positions of the oxygen centroids. The axes of this local system were oriented so that (i) its x axis was coincided with the direction of the $\mathbf{r}_{O_2O_1}^{cnt}$ vector; (ii) its z axis was oriented along the direction of the $\mathbf{r}_{H_2H_1}^{cnt} \times \mathbf{r}_{O_2O_1}^{cnt}$ vector; and (iii) its y axis was oriented according to the usual right-handed convention, namely, $\hat{y} = \hat{z} \times \hat{x}$ (here, the hat signs denote unit vectors). The results for ρ_{2D} are displayed as 3D-surface and 2D-contour plots in Figs. 5(a) and 5(b), respectively. Several observations are worth commenting: (i) as expected, the overall profile looks centrosymmetric with respect to the origin; (ii) the spatial distribution of the beads spreads along locations lying ~ 1 Å away from the positions of the two oxygen atoms, spanning the $0^\circ \lesssim \theta_i(\{\mathbf{r}_N^{(k)}\}) \lesssim 75^\circ$ interval; (iii) yet, bead distributions along these angular domains do not look uniform and clearly reveal the presence of four basins of attractions dictated by the local characteristics of the underlying potential energy surface at the transition states. Two of them [hereafter referred to as C_i ($i = 1, 2$)] are located at $\cos \theta_i \sim 1$, coinciding with connective positions; the other two (hereafter referred to as D_i) are located at $\theta_i \sim 75^\circ$ and are reminiscent of the original ones at dangling positions in reactive/product states. As expected, the basins corresponding to each H-atom are separated by local minima at the classical transition state *loci* [indicated by black dotted arrows in Fig. 5(a)]. As a result, the picture that emerges from this description can be cast in terms of stretched polymers localized at two local minima, exhibiting fleeting imaginary time transitions between C_i and D_i basins of attraction. Clearly, this scenario exhibits the basic finger prints indicative of nuclear tunneling effects.

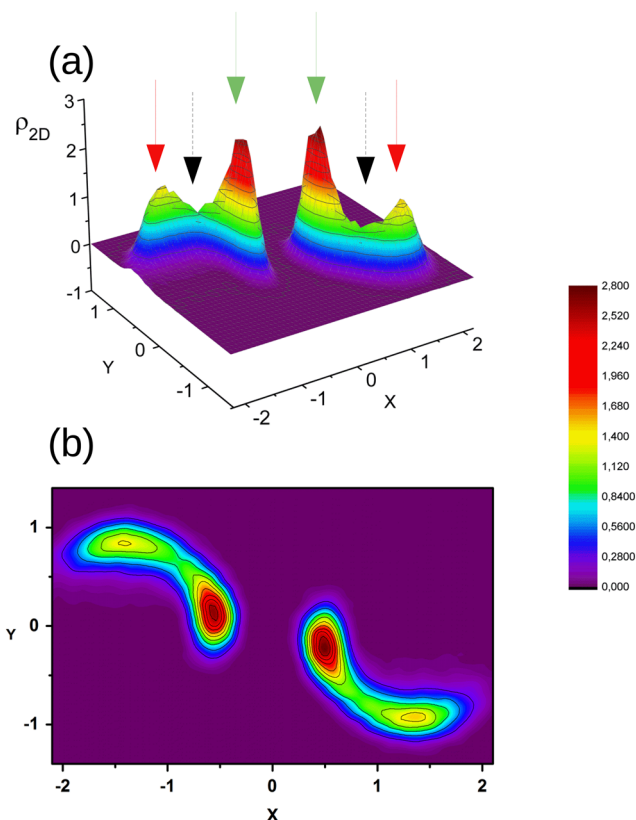


FIG. 5. 3D-surface plot (a) and 2D-contour plot (b) of the projected bead spatial density at the transition state of the W-W dimer at $T = 20$ K. Lengths are expressed in Å; ρ_{2D} is expressed in Å⁻². The solid red and green arrows in panel (a) indicate \mathcal{D} and \mathcal{C} basins of attractions, respectively. The black dotted arrows indicate H-positions at classical transition states.

The next aspect that we examined concerns the characteristics of the imaginary time concertedness of the nuclear tunneling. We started by computing probability densities for the order parameter of the type

$$P_{\xi}(\xi') = \frac{1}{P} \sum_{k=1}^P \left\langle \delta\left(\xi_k(\{\mathbf{r}_N^{(k)}\}) - \xi'\right) \right\rangle_{\xi=\xi'} \quad (19)$$

which, according to Eq. (12), were recorded for values of the centroid order parameter ξ corresponding to reactant/product, i.e., $\xi \sim \pm 1.4$, and transition, i.e., $\xi = 0$, states. In the previous equation,

$$\xi_k(\{\mathbf{r}_N^{(k)}\}) = \cos \theta_2(\{\mathbf{r}_N^{(k)}\}) - \cos \theta_1(\{\mathbf{r}_N^{(k)}\}), \quad (20)$$

which corresponds to the order parameter evaluated at the k th imaginary time slice. The plots in Fig. 6 describe bead probabilities at reactant and transition states at two different temperatures. At $T = 50$ K (red curves), both distributions look fairly localized, suggesting that the overall isomorphous polymers of the two protons retain, to a large extent, their compact shapes all along the

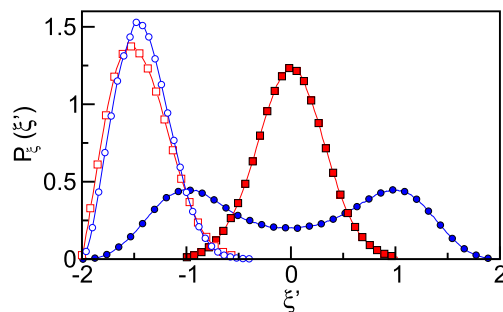


FIG. 6. Bead probability densities at the transition state [see Eqs. (19) and (20)] at $T = 50$ K (red curves) and at $T = 20$ K (blue curves). Open symbols correspond to samplings at reactive states; solid symbols correspond to samplings at transition states.

reactive path. The latter characteristics contrast sharply with the distributions evaluated at $T = 20$ K. By lowering the temperature, the symmetric gaussian-like profile registered at the transition state at $T = 50$ K transforms into a doubly peaked curve, with a depletion at $\xi' = \xi^\ddagger$. Two conclusions can be drawn from these results: (i) at $T \sim 50$ K, the particular characteristics of the intramolecular and intermolecular potentials that we adopted controlling O-H bond rotations combined the inherent quantum characteristics of the protons—expressed in terms of the magnitude of the thermally accessible spatial sampling available for the isomorphous polymers—are such that the latter exhibit several recrossings over the transition states. It is only by moving down to temperatures below, or of the order of, say, 30 K–20 K that the two tagged H-atoms exhibit clear bimodal, i.e., connective and dangling, bead-articulations; (ii) interestingly, the observation of the latter characteristics in the plots of $P_{\xi=0}(\xi)$, with local maxima located at positive and negative values of ξ , also reveals that the intermolecular interactions are established between the H-beads located at basins of attraction of different categories. Note that, for a tagged value of k , values of $\xi_k(\{\mathbf{r}_N^{(k)}\}) \sim -1$ are consistent with configurations in which $r_{H_1}^{(k)}$ lies at the \mathcal{D}_1 basin, while $r_{H_2}^{(k)}$ lies at \mathcal{C}_2 locations; conversely, values of $\xi_k(\{\mathbf{r}_N^{(k)}\}) \sim 1$ correspond to the opposite bead localizations.

The results shown in Fig. 7 illustrate the latter feature in a more clear fashion. In the bottom and top parts of the figure, we show results for $\xi_k(\{\mathbf{r}_N^{(k)}\})$ and the corresponding decomposition into $\cos \theta_i(\{\mathbf{r}_N^{(k)}\})$ ($i = 1, 2$) along the complete $0 \leq k/P \leq 1$ imaginary time interval. The results correspond to six representative, statistically independent transition state configurations that were arbitrarily time ordered so that, in all cases, $\xi(k = 0.25)$ vanishes. The plots at the top part of the figure are particularly enlightening since they reveal that the set of transition states is characterized by configurations in which $\sim 40\%$ of the H_1 beads exhibits $\cos \theta_1$ close to 1, while a similar second fraction exhibits values of $\cos \theta_1$ close to 0.1. A similar description holds for the locations of the beads in H_2 ; however, at each imaginary time slice, one observes a clear “anti-correlation” between the angular variables of the two protons. In passing, the simple inspection of the magnitude of the fluctuations at both basins indicates the more confining conditions prevailing

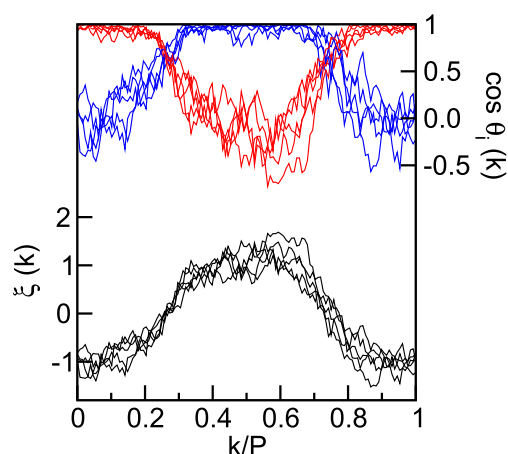


FIG. 7. Bottom panel: imaginary time collective geared exchange coordinate at the vicinity of the transition state of the W–W dimer. Top panel: imaginary time decomposition of the collective variable in terms of individual rotations. The results correspond to six statistically uncorrelated configurations, arbitrarily time aligned so that, in all cases, $\xi(k/P = 0.25) = 0$. Right axis: $\cos \theta_i$ for the same configurations. Red lines: $\cos \theta_1$ and blue lines: $\cos \theta_2$.

at C_i domains. We also remark that the interdependence observed between the positions of different particles at equal imaginary time slices can be assimilated to the generalities of a wider variety of collective proton modes describing proton transfers in ice⁴² and water autoprotolysis pathways in aqueous clusters.⁴³

The information provided in the previous paragraphs provides sufficient clues to afford a physically sound description of the nuclear quantum effects on the free energy profile of the HB donor/acceptor character exchange in terms of the following considerations: (i) starting from reactive configurations, the increments in the free energy registered along the $\xi \lesssim 0.75$ interval are mainly controlled by the energy costs required to rotate the tagged dangling proton from typically $\theta_2 \sim 115^\circ$ down to $\sim 75^\circ$. This change is accompanied by a much more modest, $\sim 15^\circ$ opposite rotation of the $O_1\text{--}H_1^{\text{con}}$ bond counterpart; (ii) these evolutions are also accompanied by rotations of the unlabeled protons in Eq. (1) that remain dangling along the complete reactive path; (iii) during this initial stage, the isomeric polymers of both protons exhibit compact structures, retaining their overall original dimensions; (iv) beyond $\xi \sim -0.75$, and at sufficiently low temperatures, a second realm prevails along which modifications in the orientations of the $O_i\text{--}H_i$ bonds, and consequently the evolution of the exchange process, are controlled by nuclear tunneling operated by concerted migrations of proton beads corresponding to equal imaginary time slices in opposite directions, i.e., connective-to-dangling (H_1) and dangling-to-connective (H_2); and (v) finally, the previous considerations naturally explain the presence of the intermediate plateau regime observed in the profile of the quantum free energy since the concerted transfers can be undertaken without involving significant modifications in the overall bead–bead intermolecular potential energy.

We close this section by briefly commenting on the modifications in the energetics involved in the exchange mechanism operated

by partial deuteration. We are referring to interconversions of the type



In Fig. 2, the corresponding free energy profile computed at $T = 20$ K is depicted with blue squares. Note that the magnitude of the barrier measured from the reactant side looks practically unchanged compared to the previous fully H scenario. Yet, the asymmetry in the isotope masses gets translated into two modifications: first, a barely discernible shift of the position of the transition state toward $\xi^{\ddagger} \sim 0.25$, along with a narrowing in the plateau-like regime, and second, and more importantly, a -0.3 kcal mol⁻¹ free energy imbalance for the net interconversion. The latter result is consistent with the thermodynamic stabilization of light isotopes at dangling positions,²⁹ which, in turn, can be rationalized in terms of the stronger spatial confinement, and consequently, higher quantum kinetic energies, at connective positions. Moreover, this propensity has been corroborated by spectroscopic signals from ice-surfaces⁴⁴ and in joint experimental–theoretical research focused on the characteristics of local isotopic densities⁴⁵ and orientational correlations at the water–vapor interface.⁴⁶

Note that an alternative interpretation of the free energy imbalance can be obtained by considering the increment in the resulting free energy barrier measured from the product side, in agreement with the ~ 0.4 kcal mol⁻¹, higher energy cost required to break D-articulated W–W bonds compared to H-articulated counterparts.^{10,47,48}

B. W–MeOH dimers

We have just showed that the mass imbalance introduced by partial deuteration is mainly translated into the thermodynamic stabilization of W–W dimers with D-articulated intermolecular connectivity. The analysis of similar exchange mechanisms in dimers combining water and methanol promotes a different kind of modification as a consequence of the asymmetries between the donor and acceptor strengths of the two species.^{49,50} Within this context, we focused attention on the following exchange isomerization:



described in terms of an order parameter similar to the one presented in Eqs. (4)–(6) [see snapshots (a)–(c) on the right-hand side of Fig. 1]. In Fig. 8, we present results for classical (black circles) and PIMD free energy plots (red open squares). At a first sight, the inspection of the plots reveals two main features: first, a 1.8 kcal mol⁻¹ classical free energy difference between reactant and product states. This difference agrees at a qualitative level with experimental evidence^{49,51} although clearly overestimates the relative stabilization when compared, for example, with predictions from quantum calculations.^{51–55} Second, and more importantly in the present context, the PIMD plot reactant and product states are bridged by a quasi-linear intermediate regime, which now replaces the aforementioned W–W plateau behavior (see plots with red open squares in the two panels).

Compared to the corresponding W–W results, the analysis of the evolutions of the O–H rotations (see blue lines in Fig. 3) and of the corresponding polymer sizes (see plots on the right-hand side

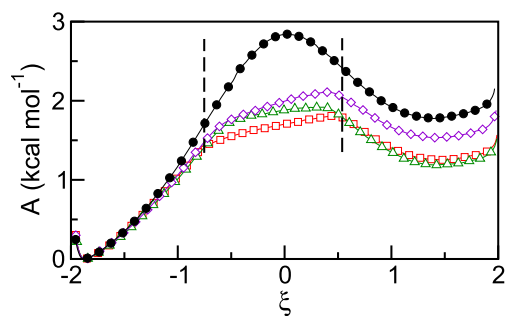


FIG. 8. Free energy profiles associated with the hydrogen bond donor/acceptor interchange for the water–methanol dimer at $T = 20$ K. Black circles: classical results; red squares: HOH–MeOH; green triangles: HOH–MeOD; and violet diamonds: HOD–MeOH. Solid symbols correspond to the classical results, whereas open symbols correspond to the path-integral results. The vertical lines indicate boundaries between quadratic and tunneling regimes.

of Fig. 4) shows no substantial modifications that might lead to microscopic interpretations of this new intermediate, linear regime. The examination of imaginary time bead correlation did prove to be more instructive. In Fig. 9, we present results for the angular variables of H_1 and H_2 along the complete $0 \leq k \leq P$ interval. For clarity purposes, the plots for the seven representative configurations are now time aligned so that $\xi(k=0)$ vanishes. The plots at the bottom part of the figure correspond to a sampling just beyond

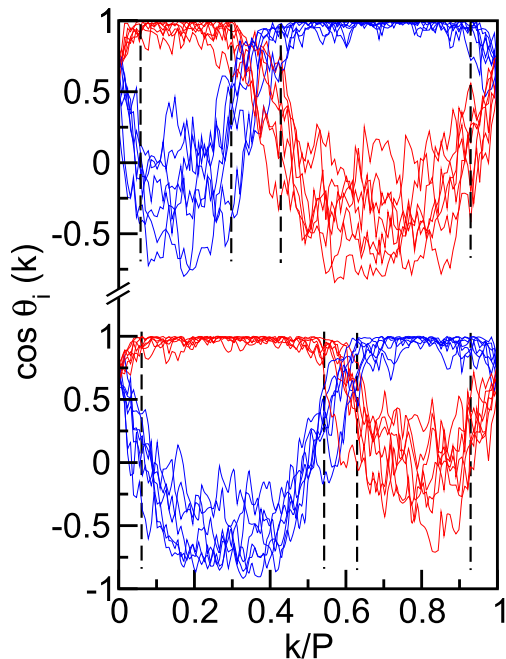


FIG. 9. Imaginary time individual rotations for configurations characterized by $\xi = -0.5$ (bottom plots) and $\xi = 0.45$ (top plots) in the W–MeOH dimer. The same labeling as the one shown in Fig. 7. Vertical dashed lines indicate boundaries for bead locations within different basins of attractions (see text).

the parabolic-to-linear transition, i.e., $\xi = -0.45$. Two stages are self-evident: along the initial, $0.05 \lesssim k/P \lesssim 0.55$ imaginary time interval, there is a clear “anticorrelation” between water-connective beads (located at the C_w basin) and methanol-dangling pseudoparticles (located at the D_{MeOH} basin); along the subsequent, $0.6 \lesssim k \lesssim 0.9$ stage, the previous trend reverses. Roughly speaking, one could conclude that, throughout this ξ realm, water–donor configurations prevail upon water–acceptor counterparts. The plots at the top correspond to a sampling at $\xi = 0.45$, just before the linear-to-parabolic crossing occurs. Here, the opposite case, dominated by larger numbers of water–acceptor/methanol–donor bead configurations, is also clearly observed. Given the energy difference that exists between these two limiting connectivities, the gradual and concerted migrations of beads between the different basins of attractions naturally provoke a linear increment of the free energy that can be ascribed to a population-weighted average between local minima of an underlying potential energy surface, with asymmetric double-well characteristics.

For the sake of completeness, we will close our analysis by briefly referring to the effects of partial deuteration on water–methanol dimers. More specifically, we are referring to the following exchange processes:



and



The plots that appear in Fig. 8 reveal that the free energy difference between reactants and products for the fully H exchange isomerization shown in Eq. (22) lies intermediate between the corresponding values of the other two isotopic variants, the largest difference being the one corresponding to the process shown in Eq. (23) (see the violet diamond plot of Fig. 8). This observation can be rationalized invoking two basic zero-point energy considerations:^{29,56} (i) regardless of the particular position considered, H-to-D transformations normally imply negative changes in free energies and (ii) moreover, free energy differences associated with isotopic changes are more marked when they are operated at connecting, i.e., more confined, positions, in contraposition to dangling positions. Armed with these arguments, let us analyze the free energy differences corresponding to exchanges involving partially deuterated water [Eq. (23)]. The latter values can be computed along an indirect path comprising three stages: the first one involves performing a reversible [$\text{D}_1^{\text{con}} \rightarrow \text{H}_1^{\text{con}}$] transformation at connective positions; the second one represents the exchange isomerization of fully H species shown in Eq. (22), whereas, during the last stage, the reverse [$\text{H}_1^{\text{dng}} \rightarrow \text{D}_1^{\text{dng}}$] transformation is operated at the dangling position. Clearly, the magnitude of the positive free energy change corresponding to the first stage surpasses the negative change registered in the last one, confirming a net increment in the free energy difference with respect to the fully H exchange.

To bring additional support to the previous qualitative considerations, we computed the free energy differences associated with the first and last steps of the previous indirect path by performing the reversible mass transformations described in Ref. 29. The procedure

relies on the previous results by Vanicek and Miller.⁵⁷ In particular, for the $[D_1^{con} \rightarrow H_1^{con}]$ transformation, we found $\Delta A_I = 1.67 \text{ kcal mol}^{-1}$, whereas, for the $[H_1^{dng} \rightarrow D_1^{dng}]$ process, we obtained $\Delta A_{III} = -1.39 \text{ kcal mol}^{-1}$. Consequently, the net free energy imbalance between the violet-diamond and red-square plots obtained from the mass transformation is $\Delta A = \Delta A_{III} + \Delta A_I = 0.28 \text{ kcal mol}^{-1}$.

Invoking similar arguments, the tandem



necessarily leads to lower free energy differences. In this case, our simulations yielded $\Delta A_I = 1.51 \text{ kcal mol}^{-1}$ and $\Delta A_{III} = -1.65 \text{ kcal mol}^{-1}$, which leads to a net $\Delta A = -0.14 \text{ kcal mol}^{-1}$ additional stabilization of the product state. Note that in the two cases, the numerical results agree reasonably well with the results obtained by building up the complete free energy plots shown in Fig. 8.

IV. CONCLUDING REMARKS

The PIMD simulation results presented in this paper reveal that the explicit incorporation of nuclear quantum fluctuations gives rise to important modifications in the landscape of the free energy associated with the HB donor/acceptor exchange in the W–W dimer. At cryogenic temperatures of about $\sim 50 \text{ K}$, tunneling effects are moderate and the main changes are manifested by a sensible reduction in the magnitude of the free energy barrier. Still, the overall shape of the profile maintains the bistable characteristics of the classical curve and the isomorphous polymers exhibit a fairly compact structure. Much more dramatic modifications take place by lowering the temperature even further. At temperatures of the order of 20 K , the free energy plot exhibits three stages with well differentiated characteristics: at the vicinities of reactant and product states, the profile retains its original quadratic characteristics. Along these limiting stages, the isomorphous proton-polymers still resemble wounded moieties and the reactive path is operated by a geared internal rotation of the dangling-H in the acceptor molecule with respect to the connecting-H in the donor partner. These concerted rotations, though, evolve at different paces, revealing the more confining characteristics of the underlying potential energy surface at connecting positions. Sharp transitions into an intermediate plateau regime occur at $\xi \pm 0.5$, along which the mechanism is controlled by nuclear tunneling operated by gradual migrations of polymer beads from different basins of attractions in a concerted fashion. The analysis of imaginary time correlations between bead localizations at the transition states shows that these transfers are brought about along opposite directions and, as such, do not require meaningful energy costs. Asymmetries introduced by partial deuteration do not modify the previous description at a qualitative level. Still, the simulations corroborate the more marked thermodynamic stability of light isotopes at dangling positions in contraposition with connecting ones. Although this qualitative trend could be anticipated based on zero-point considerations,²² numerical estimates of the free energy differences, adequately converted into isomer populations or, equivalently, spectral intensities, could provide information to estimate cluster temperatures, which are normally of difficult detection.²⁹

The analysis of the asymmetries introduced by replacing one of the W-partners by MeOH does provide additional insights. In this case, the gross features of the differences between the acceptor and donor strengths of the two species are reflected in differences between the confining characteristics of the corresponding basins of attractions of each partner. Invoking a similar migration mechanism, the energy costs involved in the transfer of beads from connecting-to-dangling realms in the W donor surpass the ones required for the opposite transfers in the acceptor MeOH. Consequently, the origins of the intermediate linear regime joining reactant and product states are the result of a population-weighted average of an effective asymmetric potential. The consideration of basic elements combining zero-point energy arguments and a simple indirect thermodynamic cycle provides plausible arguments to justify that the free energy difference between reactants and products for the fully H exchange isomerization is intermediate between the other two differences corresponding to partially deuterated partners. We have corroborated this feature from an alternative quantitative route by performing the reversible mass transformations at reactant and product states.

The free energy profiles that we examined are the result of an approximate sampling procedure based on an order parameter defined in terms of centroid coordinates. Consequently, given the highly nonlinear nature of the latter parameter, such implementation is likely to neglect a part of quantum fluctuations originated in the spatial delocalization of protons. Nevertheless, our results have important implications at the time to estimate rates for the exchange process. For example, centroid-based free energies represent an essential ingredient within the ring-polymer-molecular-dynamics methodology to evaluate quantum rates from flux-side correlation functions.^{38,59} This is particularly relevant in the present deep tunneling context where the estimates obtained from the latter approach are known to be accurate.⁶⁰

To conclude, we will briefly comment on a technical issue concerning the choice of the force field that we implemented. It is well documented that the dissociation energies for the water dimer obtained from the most widely used pseudopotentials, normally tailored to reproduce bulk water properties, are higher than the experimental results,^{61,62} in this respect, the q-TIP4P/F parameterization makes no exception.¹⁰ In addition, similar trends are registered in the W–MeOH dimer case. As a result, from quantitative grounds, the free energy barriers that appear in Figs. 2 and 8 are likely to be also overestimated. In the present case, we refrained from implementing more elaborate models for water dimer potential^{20,21,48} to maintain a uniform level of description between water–water and water–methanol interactions. Nevertheless, we have no elements that might lead us to suspect that the physical picture that emerges from our results may include artifacts originated in the deficiencies of the potential models. In fact, imaginary time correlations between intermolecular bead-to-bead interactions, similar to ones presented here, have also been reported in simulations that implemented much more elaborate *ab initio* molecular dynamics schemes.⁴² As such, we believe that our description captures the basic elements that distinguish quantum from classical descriptions of the free energy profiles. We are currently pursuing a new parameterization of the methanol force field that may lead to an improvement in the agreement between simulation and direct experimental results.

SUPPLEMENTARY MATERIAL

Details of the force field for MeOH are presented in the [supplementary material](#).

ACKNOWLEDGMENTS

E.M. is a recipient of a graduate fellowship from CONICET, Argentina. D.L. is a staff member of CONICET, Argentina.

DATA AVAILABILITY

The data that support the findings of this study are available from the corresponding author upon reasonable request.

REFERENCES

- 1 T. R. Dyke, *J. Chem. Phys.* **66**, 492 (1977).
- 2 D. J. Wales, "Rearrangements of water dimer and hexamer," in *Theory of Atomic and Molecular Clusters with a Glimpse at Experiments*, edited by J. Jellinek (Springer, New York, 1999), p. 86.
- 3 J. B. Paul, R. A. Provencal, and R. J. Saykally, *J. Phys. Chem. A* **102**, 3279 (1998).
- 4 J. B. Paul, R. A. Provencal, C. Chappo, A. Petterson, and R. J. Saykally, *J. Chem. Phys.* **109**, 10201 (1998).
- 5 N. Goldman and R. Saykally, *J. Chem. Phys.* **120**, 4777 (2004).
- 6 A. Mukhopadhyay, S. S. Xantheas, and R. J. Saykally, *Chem. Phys. Lett.* **700**, 163 (2018).
- 7 S. C. Althorpe and D. C. Clary, *J. Chem. Phys.* **101**, 3603 (1994).
- 8 J. K. Gregory and D. C. Clary, *J. Chem. Phys.* **102**, 7817 (1995).
- 9 T. S. Cole and R. J. Saykally, *J. Chem. Phys.* **147**, 064301 (2017).
- 10 M. Schimdt and P.-N. Roy, *J. Chem. Phys.* **148**, 124116 (2018).
- 11 M. W. Kirova, *Phys. Chem. Chem. Phys.* **18**, 27351 (2016).
- 12 B. J. Smith, D. J. Swanton, J. A. Pople, H. F. Schaefer III, and L. Radom, *J. Chem. Phys.* **92**, 1240-1247 (1990).
- 13 J. O. Richardson, S. C. Althorpe, and D. J. Wales, *J. Chem. Phys.* **135**, 124109 (2011).
- 14 J. O. Richardson, *J. Chem. Phys.* **148**, 200901 (2018).
- 15 J. O. Richardson, C. Pérez, S. Lobsiger, A. A. Reid, B. Temelso, G. C. Shields, Z. Kisiel, D. J. Wales, B. H. Pate, and S. C. Althorpe, *Science* **351**, 1310 (2016).
- 16 C. Vaillant, S. C. Althorpe, and D. J. Wales, *J. Chem. Theory Comput.* **15**, 33 (2019).
- 17 C. L. Vaillant, D. J. Wales, and S. C. Althorpe, *J. Phys. Chem. Lett.* **10**, 7300 (2019).
- 18 C. L. Vaillant, D. J. Wales, and S. C. Althorpe, *J. Chem. Phys.* **148**, 234102 (2018).
- 19 C. L. Vaillant and M. T. Cvitaš, *Phys. Chem. Chem. Phys.* **20**, 26809 (2018).
- 20 X. Huang, B. J. Braams, J. M. Bowman, C. L. Emerson, R. E. A. Kelly, J. Tenynson, G. C. Groenenboom, and A. van der Avoird, *J. Chem. Phys.* **128**, 034312 (2008).
- 21 V. Babin, C. Leforestier, and F. Paesani, *J. Chem. Theory Comput.* **9**, 5395 (2013).
- 22 E. G. Diken, J.-W. Shin, E. A. Price, and M. A. Johnson, *Chem. Phys. Lett.* **387**, 17 (2004).
- 23 S. Horvath, A. B. McCoy, B. M. Elliott, G. H. Weddle, J. R. Roscioli, and M. A. Johnson, *J. Phys. Chem. A* **114**, 1556 (2010).
- 24 P. E. Videla, P. J. Rossky, and D. Laria, *J. Phys. Chem. B* **119**, 11783 (2015).
- 25 M. E. Tuckerman and A. Hughes, in *Classical and Quantum Dynamics in Condensed Phase Simulations*, edited by B. J. Berne, G. Ciccotti, and D. F. Coker (World Scientific, Singapore, 1998), Chap. 14.
- 26 M. E. Tuckerman, in *Statistical Mechanics: Theory and Molecular Simulation* (Oxford University Press, 2010), Chap. 10.
- 27 D. Chandler and P. G. Wolynes, *J. Chem. Phys.* **74**, 4078 (1981).
- 28 S. Habershon, T. E. Markland, and D. E. Manolopoulos, *J. Chem. Phys.* **131**, 024501 (2009).
- 29 P. E. Videla, P. J. Rossky, and D. Laria, *J. Phys. Chem. Lett.* **5**, 2375 (2014).
- 30 P. E. Videla, P. J. Rossky, and D. Laria, *J. Chem. Phys.* **139**, 174315 (2013).
- 31 P. E. Videla, P. J. Rossky, and D. Laria, *J. Chem. Phys.* **148**, 084303 (2018).
- 32 T. Honma, C. C. Liew, H. Inomata, and K. Arai, *J. Phys. Chem. A* **107**, 3960 (2003).
- 33 S. Habershon, G. S. Fanourgakis, and D. E. Manolopoulos, *J. Chem. Phys.* **129**, 074501 (2008).
- 34 A. Witt, S. D. Ivanov, M. Shiga, H. Forbert, and D. Marx, *J. Chem. Phys.* **130**, 194510 (2009).
- 35 G. J. Martyna, M. E. Tuckerman, D. J. Tobias, and M. L. Klein, *Mol. Phys.* **87**, 1117 (1996).
- 36 M. Ceriotti, M. Parrinello, T. E. Markland, and D. E. Manolopoulos, *J. Chem. Phys.* **133**, 124104 (2010).
- 37 P. E. Videla, P. J. Rossky, and D. Laria, *J. Chem. Phys.* **144**, 061101 (2016).
- 38 D. Frenkel and B. Smit, in *Understanding Molecular Simulation: From Algorithms to Applications* (Academic Press, 2001), Chap. 7.
- 39 K. P. Bishop and P.-N. Roy, *J. Chem. Phys.* **148**, 102303 (2018).
- 40 S. Habershon and D. E. Manolopoulos, *J. Chem. Phys.* **135**, 224111 (2011).
- 41 A. L. Nichols, D. Chandler, Y. Singh, and D. M. Richardson, *J. Chem. Phys.* **81**, 5109 (1984).
- 42 C. Drechsel-Grau and D. Marx, *Phys. Rev. Lett.* **112**, 148302 (2014).
- 43 L. Turi, J. Rodriguez, and D. Laria, *J. Phys. Chem. B* **124**, 2198 (2020).
- 44 J. P. Devlin, *J. Chem. Phys.* **112**, 5527 (2000).
- 45 J. Liu, R. S. Andino, C. M. Miller, X. Chen, D. M. Wilkins, M. Ceriotti, and D. E. Manolopoulos, *J. Phys. Chem. C* **117**, 2944 (2013).
- 46 Y. Nagata, R. E. Pool, E. H. G. Backus, and M. Bonn, *Phys. Rev. Lett.* **109**, 226101 (2012).
- 47 B. Ruscic, *J. Phys. Chem. A* **117**, 11940 (2013).
- 48 L. C. Ch'ng, A. K. Samanta, G. Czako, J. M. Bowman, and H. Reisler, *J. Am. Chem. Soc.* **134**, 15430 (2012).
- 49 M. Nedić, T. N. Wassermann, R. W. Larsen, and M. A. Suhm, *Phys. Chem. Chem. Phys.* **13**, 14050 (2011).
- 50 C. Emmeluth, V. Dyczmons, and M. A. Suhm, *J. Phys. Chem. A* **110**, 2906 (2006).
- 51 P. A. Stockman, G. A. Blake, F. J. Lovas, and R. D. Suenram, *J. Chem. Phys.* **107**, 3782 (1997).
- 52 B. S. Jursic, *J. Mol. Struct.: THEOCHEM* **466**, 203 (1999).
- 53 Y.-F. Lee, A.-M. Kelterer, G. Matisz, S. Kunsági-Máté, C.-Y. Chung, and Y.-P. Lee, *J. Chem. Phys.* **146**, 144308 (2017).
- 54 A. Mandal, M. Prakash, R. M. Kumar, R. Parthasarathi, and V. Subramanian, *J. Phys. Chem. A* **114**, 2250 (2010).
- 55 J. W. Moskowitz, Z. Bačić, A. Sarsa, and K. E. Schmidt, *J. Chem. Phys.* **114**, 10294 (2001).
- 56 M. Ceriotti and T. Markland, *J. Chem. Phys.* **138**, 014112 (2013).
- 57 J. Vanicek and W. H. Miller, *J. Chem. Phys.* **127**, 114309 (2007).
- 58 J. O. Richardson and S. C. Althorpe, *J. Chem. Phys.* **131**, 214106 (2009).
- 59 S. Habershon, D. E. Manolopoulos, T. E. Markland, and T. F. Miller III, *Annu. Rev. Phys. Chem.* **64**, 387 (2013).
- 60 I. R. Craig and D. Manolopoulos, *J. Chem. Phys.* **123**, 034102 (2005).
- 61 T. James, D. J. Wales, and J. Hernández-Rojas, *Chem. Phys. Lett.* **415**, 302 (2005).
- 62 A. Glaättili, X. Daura, and W. F. van Gunsteren, *J. Chem. Phys.* **116**, 9811 (2002).